ROYAL SOCIETY OF CHEMISTRY

PAPER

Mesoporous Mn₃O₄–CoO core–shell spheres wrapped by carbon nanotubes: a high performance catalyst for the oxygen reduction reaction and CO oxidation†

Junwu Xiao,‡*[a] Lian Wan,‡[a] Xue Wang,[b] Qin Kuang,[b] Shuang Dong,[a] Fei Xiao[a] and Shuai Wang*[a]

The controllable synthesis of transition metal oxide nanomaterials has attracted considerable attention for the replacement of the current precious metal catalysts. Herein, we have developed a facile method to successfully synthesize Mn_3O_4–CoO core–shell mesoporous spheres, which are wrapped by carbon nanotubes (CNT), and investigated the catalytic activity for the oxygen reduction reaction (ORR) and CO oxidation for the first time. The ORR process on the Mn_3O_4–CoO/CNT catalysts was via a complete oxygen reduction process ($4e^-$), and the catalytic activity was far better than for the Mn_3O_4/CNT and CoO/CNT catalysts. The durability even out-performed the commercial Pt/C catalysts. As compared with the Mn_3O_4/CNT and CoO/CNT catalysts, the Mn_3O_4–CoO/CNT catalysts also exhibited better catalytic activity for CO oxidation. The initial and complete conversion temperatures for the Mn_3O_4–CoO/CNT catalysts can decrease to 30 and 120 °C, respectively. The good catalytic activity for the ORR and CO oxidation is due to the high specific surface area (138.9 m^2 g^{-1}) provided which gives many catalytically active sites, mesoporous structure (15 to 120 nm) favoured for molecule accessibility to the active surface of the nanocrystals and mass transport, and the synergistic catalytic effect of Mn_3O_4 and CoO catalytically active sites.

Introduction

Transition metal oxides have received considerable interest as a class of materials because of their wide applications. One such application is due to their catalytic properties, which have attracted remarkable attention, since the present catalysts are usually rare and precious metals such as Pt, Au and Pd. The commercial catalyst for the sluggish oxygen reduction reaction (ORR) in fuel cells and metal–air batteries is Pt nanoparticles supported on high surface area carbon.[1] Owing to the high cost of Pt and the insufficient activity, non-precious catalysts such as metal–N complexes on carbon matrixes,[2,3] perovskite- and

spinel-type metal oxides,[4–8] and doped carbonaceous materials[9] have been recently identified for catalysing the ORR.

Transition metal oxides, such as manganese oxides and cobalt oxides, are thought of as some of the promising non-precious ORR catalysts. Cobalt oxides, such as Co_3O_4 and CoO, anchored on carbonaceous materials (graphene and carbon nanotubes), have exhibited excellent ORR catalytic activity.[5,7,10,11] Similarly high catalytic activity has been reported for manganese oxides, which are inexpensive, earth-abundant and environmentally benign. Manganese oxides can come in a variety of forms, many of which have been shown as high-performing catalysts for the ORR, such as γ-MnOOH,[12] α-Mn_2O_3,[13] α-MnO_2,[14,15] Mn_3O_4,[16] birnessite–MnO_2[17] and β-MnO_2.[18] Manganese oxides and cobalt oxides have also been reported as efficient catalysts for CO oxidation. Co_3O_4 nanorods and nanosheets can catalyse CO oxidation at a relatively low temperature, which is attributed to the high density of active Co^{3+} cations on the exposed crystal faces.[19–22] The catalytic activity of CO oxidation on manganese oxide catalysts is dependent on the polymorphism and valence states of the exposed Mn cations, since the specific surface termination is the determining factor.[23–25] As compared with pristine manganese oxide and cobalt oxide catalysts, integrating manganese oxides with cobalt oxides, for example $MnCo_2O_4$ and Mn_3O_4 in

[a]College of Chemistry and Chemical Engineering, Hubei Key Laboratory of Material Chemistry and Service Failure, Key Laboratory for Large-Format Battery Materials and System, Ministry of Education, Huazhong University of Science & Technology, Wuhan, PR China. E-mail: chjwxiao@hust.edu.cn; chmsamuel@hust.edu.cn

[b]Department of Chemistry, College of Chemistry and Chemical Engineering, Xiamen University, Xiamen, 361005, PR China

† Electronic supplementary information (ESI) available: XRD pattern, FT-IR spectra, N_2 adsorption–desorption curve, EDX results, TEM image of the CoO/CNT nanocomposites, a series of rotating disk voltammograms of the oxygen reduction reaction in O_2-saturated 0.1 M KOH electrolyte, and TGA results. See DOI: 10.1039/c3ta14453d

‡ They are co-first authors.

3794 | J. Mater. Chem. A, 2014, 2, 3794–3800

This journal is © The Royal Society of Chemistry 2014

Co_3O_4 microspheres, can further improve the catalytic activity for both the ORR and CO oxidation.[24,26] Thus, catalytically active Mn and Co sites cooperatively enhance the catalytic activity. However, the current catalyst materials for the ORR and CO oxidation are still far from meeting the requirements of combined high catalytic activity, strong durability and low cost. New strategies to develop high performance catalysts are still desirable.

Herein, we have developed a new strategy to develop Mn_3O_4–CoO core–shell mesoporous spheres, which were wrapped by CNTs. Owing to the high specific surface area, mesoporous structure and the synergistic catalytic effect of Mn_3O_4 and CoO, the Mn_3O_4–CoO/CNT nanocomposite catalyst exhibited improved catalytic activity for the ORR and CO oxidation.

Experimental

Preparation of the well dispersed carbon nanotube (CNT) solution

The well dispersed CNT solution was obtained *via* a mixed acid treatment. Specifically, 1 g of hydroxylated CNTs were firstly dispersed in 30 mL concentrated sulfuric acid and 10 mL nitric acid, and refluxed at 100 °C for 1.5 h. Then, after cooling down to room temperature, the deionized (DI) water was added to the solution until no heat was released. The resulting mixture was centrifuged for 10 min at 14 000 rpm to separate out the product, and was washed by distilled water twice. Finally the precipitates were well dispersed in 200 mL of DI water with a concentration of ~1.3 mg mL^{-1} and a pH value of ~1.0.

Synthesis of the Mn_3O_4/CNT, CoO/CNT and Mn_3O_4–CoO/CNT nanocomposites

The Mn_3O_4/CNT nanocomposites were produced by a direct redox reaction between the CNTs and $KMnO_4$, and the subsequent thermal treatment process. Firstly, 50 mL of 0.01 M $KMnO_4$ solution was heated to 70 °C, and then 20 mL of the as-prepared CNT solution was added to the solution. The reaction was carried out at 70 °C for 2.0 h. The suspension was centrifuged and washed with DI water, and then freeze dried to obtain the Mn salt/CNT products. Finally, the products were thermally treated at 400 °C for 1.0 h under a N_2 atmosphere, with a heating rate of 5 °C min^{-1}, to form the Mn_3O_4/CNT nanocomposites.

For preparing the Mn_3O_4–CoO/CNT nanocomposites, firstly 5 mM $CoCl_2$ and 10 mM $NaHCO_3$ were dissolved in 100 mL of H_2O, and flushed with gaseous CO_2 for 2.0 h, forming the supersaturated cobalt bicarbonate solution. Then, 0.15 g of the Mn salt/CNT products was dispersed in the above solution. After stirring at room temperature for 12.0 h, the precipitates were centrifuged, washed with DI water, and then freeze dried. Finally, the products were thermally treated at 400 °C for 1.0 h under a N_2 atmosphere, with a heating rate of 5 °C min^{-1}, to form the Mn_3O_4–CoO/CNT nanocomposites.

The formation process of the CoO/CNT nanocomposites was described as follows: to start with, 10 mM of $CoCl_2 \cdot 6H_2O$ and 20 mM of $NaHCO_3$ were dissolved in 80 mL of DI water and mixed with 20 mL of the well dispersed CNT solution. The mixture was flushed with gaseous CO_2 for 2.0 h, forming a transparent CNT/supersaturated cobalt bicarbonate solution. After stirring at room temperature for 12 h, the precipitates were collected *via* centrifugation, washed with DI water, and then freeze dried. Finally, the precipitates were thermally decomposed at 400 °C for 1.0 h under a N_2 atmosphere, with a heating rate of 5 °C min^{-1}, to form the CoO/CNT nanocomposites.

General characterization

The product morphologies were directly examined by scanning electron microscopy (SEM) using a JEOL JSM-6700F instrument at an accelerating voltage of 5 kV. Transmission electron microscopy (TEM) observations were carried out on a JEOL 2010 microscope operating at 200 kV. X-ray diffraction (XRD) was performed on a Philips PW-1830 X-ray diffractometer with Cu Kα irradiation ($\lambda = 1.5406$ Å). The step size and scan rate were set as 0.05° and 0.025° s^{-1}, respectively. X-ray photoelectron spectroscopy (XPS) was measured on a Perkin-Elmer model PHI 5600 XPS system with a resolution of 0.3–0.5 eV from a mono-chromated aluminum anode X-ray source with Kα radiation (1486.6 eV). Brunauer–Emmett–Teller (BET) surface areas were measured on a Coulter SA 3100 surface area analyser. Fourier transform infrared spectroscopy (FT-IR) was carried out on a Bruker Vertex 70 instrument. The inductively coupled plasma atomic emission spectroscopy (ICP-AES) was measured on an Agilent Technologies 4100 MP-AES instrument. Thermogravimetric analysis (TGA) was performed from 50 to 700 °C on a TGA Q 5000 (TA Instruments Ltd.) at a heating rate of 5 °C min^{-1} under an air flow of 25 mL min^{-1}.

Catalytic measurements for the oxygen reduction reaction (ORR)

Electrochemical measurements were carried out by cyclic voltammetry (CV) on a CHI 660E electrochemical workstation. A conventional, three-electrode cell was used, consisting of a glassy carbon electrode (GCE) with an area of 0.125 cm^2 as the working electrode, Pt foil as the counter electrode and Hg/HgO (1.0 M KOH) (MMO, 0.098 V *vs.* SHE) as the reference electrode. The working electrode was modified with a catalyst layer by dropping a suitable amount of catalyst ink on the GCE. The catalyst ink was prepared by ultrasonically dispersing 10 mg of the samples in a 2.0 mL solution (1.9 mL of ethanol and 0.1 mL of 5 wt% Nafion solution) for 30 min to obtain a homogeneous solution. 10 μL of the dispersion was dropped onto the GCE, which was then dried in air. CV and polarization curves for the ORR were obtained in 0.1 M KOH solution using the rotating disk electrode (RDE-3A). Before the RDE study, the electrodes were cycled at 50 mV s^{-1} between 0.2 and −0.6 V until reproducible cyclic voltammograms were obtained. Normalized currents are given in terms of the geometric weight (mA cm^{-2}). The working electrode was scanned cathodically at a rate of 5 mV s^{-1}, varying the rotating speed from 400 to 2400 rpm. Koutecky–Levich plots (J^{-1} *vs.* $\omega^{-1/2}$) were analysed at various electrode potentials. The slopes of their best linear fit lines were

This journal is © The Royal Society of Chemistry 2014

J. Mater. Chem. A, 2014, **2**, 3794–3800 | 3795

used to calculate the number of electrons transferred (n) on the basis of the Koutecky–Levich equation:

$$\frac{1}{J} = \frac{1}{J_k} + \frac{1}{J_L} = \frac{1}{J_k} + \frac{1}{B\omega^{1/2}} \tag{1}$$

$$B = 0.62nFC_oD_o^{2/3}\nu^{-1/6} \tag{2}$$

$$J_k = nFkC_o \tag{3}$$

where J is the measured current density, J_k and J_L are the kinetic- and diffusion-limiting current densities, ω is the angular velocity, n is the transferred electron number, F is the Faraday constant (96 485 C mol^{-1}), C_o is the bulk concentration of O_2 (1.2×10^{-6} mol cm^{-3}), ν is the kinematic viscosity of the electrolyte (0.01 cm^2 s^{-1}), D_o is the O_2 diffusion coefficient (1.9×10^{-5} cm^2 s^{-1}) and k is the electron-transfer rate constant.

Catalytic measurements for CO oxidation

The reaction gas, 5% CO in nitrogen (99.999% purity) (10 mL min^{-1}) and air (99.999% purity) (40 mL min^{-1}), was fed to the catalysts (30 mg), which was set in a fixed-bed flow reactor made of glass with an inner diameter of 2.4 mm. The steady-state catalytic activity was measured at each temperature, with the reaction temperature rising from room temperature to 320 °C. The effluent gas was analysed on-line by an on-stream gas chromatograph (Ramiin GC 2060) equipped with a TDX-01 column.

The H$_2$-temperature programmed reduction (H$_2$-TPR) measurements were carried out on a Micromeritics Auto Chem II 2920 instrument. Firstly, ~100 mg catalyst was placed in the U-type quartz tube, and pre-treated under an Ar atmosphere at 473 K for 0.5 h. Then, after cooling down to room temperature, the samples were placed in a TPR cell, into which the H$_2$–Ar (5 : 95) mixed gas was introduced. The temperature was programmed to rise at a constant rate of 10 K min^{-1}. The amount of H$_2$ uptake during the reduction was detected by a thermal conductivity detector (TCD).

Results and discussion

The formation process of the Mn$_3$O$_4$/CNT, CoO/CNT and Mn$_3$O$_4$–CoO/CNT nanocomposites is schematically shown in Fig. 1. For synthesizing the Mn$_3$O$_4$/CNT and Mn$_3$O$_4$–CoO/CNT nanocomposites, firstly carbon nanotubes (CNTs), as the reducing agent, reacted with KMnO$_4$ solution to form K$_{0.27}$MnO$_2$·0.54H$_2$O (Step I in Fig. 1), of which the XRD pattern is consistent with the standard pattern JCPDS 86-0666 (Fig. SI-1A†) and the literature.[27] The as-formed K$_{0.27}$MnO$_2$ nanomaterials exhibited flower-like sphere shapes, and were composed from the aggregation of nanosheets (Fig. 2A and B). Together with the SEM and TEM images (Fig. SI-2A and B†), we can clearly see that the remaining CNTs were attached on the flower-like K$_{0.27}$MnO$_2$ spheres. The force between them may be the COO–M (M = K, Mn) interaction, which can be seen from the asymmetric and symmetric stretching vibration frequencies of C=O in the K$_{0.27}$MnO$_2$·0.54H$_2$O/CNT nanocomposites

shifting to lower wavenumbers, as compared with those in the pristine CNTs (Fig. SI-2B†). The lattice fringes with interlayer distances of 0.34 and 0.72 nm in the high resolution TEM (HRTEM) image belong to CNTs and K$_{0.27}$MnO$_2$·0.54H$_2$O, respectively (Fig. 2C), further suggesting that the CNTs are adsorbed on the K$_{0.27}$MnO$_2$ spheres. After the thermal decomposition process, the K$_{0.27}$MnO$_2$·0.54H$_2$O precursors were transformed to Mn$_3$O$_4$ with the conserved sphere morphology (Step II in Fig. 1 and Fig. SI-1B†), but the component nanosheets were decomposed into nanoparticles, accompanied with the loss of the crystalline water (Fig. 2D and E). The lattice fringes with interlayer distances of 0.25 and 0.49 nm can be ascribed to the lattice distances of the (211) and (101) crystal faces of Mn$_3$O$_4$, respectively (Fig. 2F). The porous characteristics of the Mn$_3$O$_4$/CNT nanocomposites were investigated via Brunauer–Emmett–Teller (BET) gas sorption measurements. The specific surface area was ~186.2 m^2 g^{-1}, and the corresponding Barrett–Joyner–Halenda (BJH) pore sizes were distributed from 15 to 60 nm, as calculated from the N$_2$ adsorption–desorption isotherms (Fig. SI-3†).

After dispersion in the supersaturated cobalt bicarbonate solution for 12 h, the cobalt salts were grown on the surface of K$_{0.27}$MnO$_2$, forming K$_{0.27}$MnO$_2$·0.54H$_2$O–cobalt salt spheres (Step III in Fig. 1 and Fig. 3A–C). During the subsequent thermal treatment process (Step IV in Fig. 1), the cobalt salt and K$_{0.27}$MnO$_2$·0.54H$_2$O precursors were decomposed into CoO and Mn$_3$O$_4$, respectively (Fig. SI-1C†), forming Mn$_3$O$_4$–CoO spheres (Fig. 3D and E). The lattice fringes with interlayer distances of 0.25 and 0.42 nm at the edge of the spheres correspond to the lattice distances of the (111) and (100) crystal faces of CoO (Fig. 3F), indicating that CoO is mainly located in the outer layer of the spheres. The EDX results showed that the Mn and Co elements are dominant at the centre and edges of the spheres, respectively (Fig. SI-4†). It indicates that the Mn$_3$O$_4$–CoO spheres featured a core–shell structure. The specific surface area of the Mn$_3$O$_4$–CoO spheres was 138.9 m^2 g^{-1}, smaller than that of the Mn$_3$O$_4$ spheres, since the pore sizes expanded from 15–60 to 15–120 nm (Fig. SI-3†). When only the CNTs were dispersed on the supersaturated cobalt bicarbonate solution, the cobalt salt precursors were grown on the CNTs, forming the Co salts/CNT precursors, similar with those grown on graphene sheets,[28] and then thermally decomposed into the CoO/CNT composites (Step V in Fig. 1, and Fig. SI-1D and SI-5†).

The composition of the Mn$_3$O$_4$/CNT, CoO/CNT and Mn$_3$O$_4$–CoO/CNT composites was investigated by inductively coupled plasma atomic emission spectroscopy (ICP-AES) and X-ray photoelectron spectroscopy (XPS) (Fig. 4). The contents of Mn$_3$O$_4$, CoO and Mn$_3$O$_4$–CoO in the composites were 66.9 wt%, 62.2 wt%, and 79.0 wt%, respectively. The Mn/Co molar ratio in the Mn$_3$O$_4$–CoO/CNT composites was 1.2 : 1. The C 1s XPS spectrum was fitted according to the following carbon bonding environments: 284.5 (C–C), 285.7 (C–O–C and C–O–H), and 290.5 eV (O–C=O) (Fig. 4A). The peaks at 529.8, 531.1 and 532.9 eV in the O 1s spectrum correspond to the O 1s signal of the oxides (Mn$_3$O$_4$ and CoO), the COO–Mn$_3$O$_4$/CoO interfacial bonding structure and the residual oxygen-containing groups (such as –OH and –COOH), respectively (Fig. 4B). The 2p$_{3/2}$ and
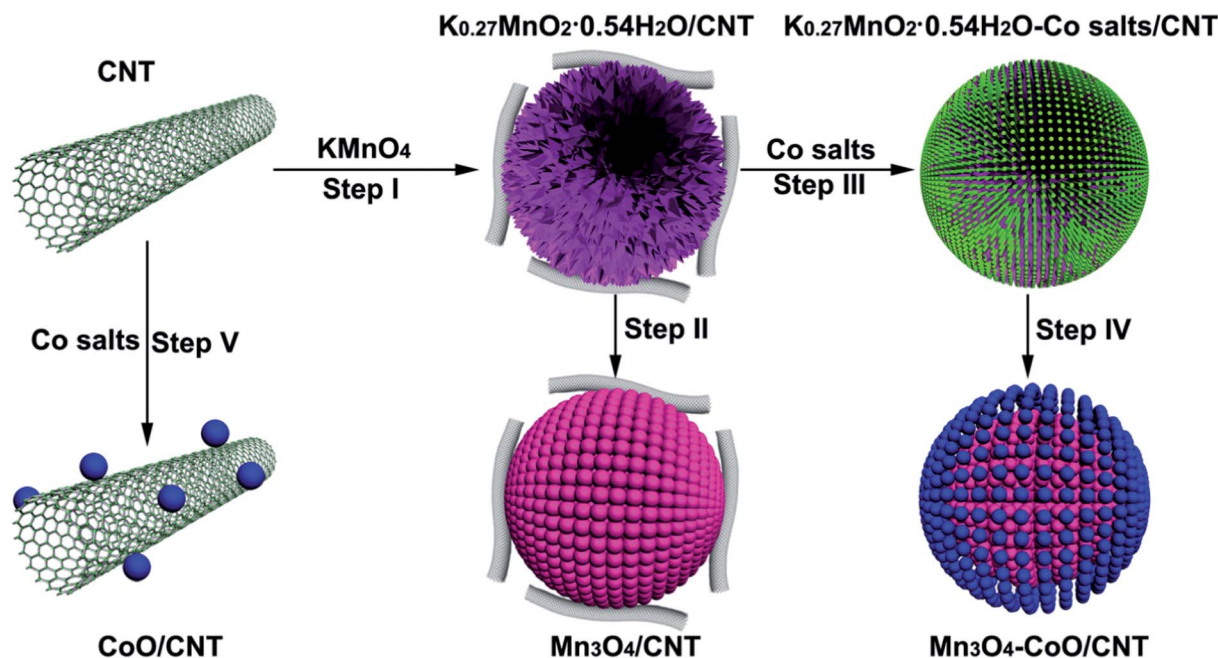
3796 | J. Mater. Chem. A, 2014, **2**, 3794–3800

This journal is © The Royal Society of Chemistry 2014

Fig. 1 Schematic graph of the formation process of the Mn_3O_4/CNT, CoO/CNT and Mn_3O_4–CoO/CNT nanocomposites. CNTs reacted with $KMnO_4$ to form the $K_{0.27}MnO_2 \cdot 0.54H_2O$ precursors (Step I), which were then thermally decomposed into the Mn_3O_4/CNT nanocomposites (Step II). When the $K_{0.27}MnO_2 \cdot 0.54H_2O$ precursors were dispersed in the supersaturated cobalt bicarbonate solution, the cobalt salt nanocrystals were grown on the $K_{0.27}MnO_2 \cdot 0.54H_2O$ spheres with the loss of CO_2, forming the $K_{0.27}MnO_2 \cdot 0.54H_2O$–Co salt core–shell spheres (Step III). The $K_{0.27}MnO_2 \cdot 0.54H_2O$–Co salt precursors were thermally decomposed into the Mn_3O_4–CoO/CNT nanocomposites (Step IV). The cobalt salt precursors can be directly formed on the CNTs from the supersaturated cobalt bicarbonate solution with the loss of CO_2, and were then thermally decomposed into the CoO/CNT nanocomposites (Step V).
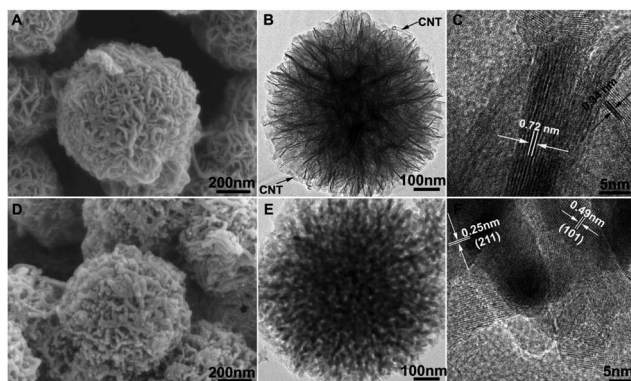

Fig. 2 SEM and TEM images of the (A–C) $K_{0.27}MnO_2 \cdot 0.54H_2O$/CNT and (D–F) Mn_3O_4/CNT nanocomposites.
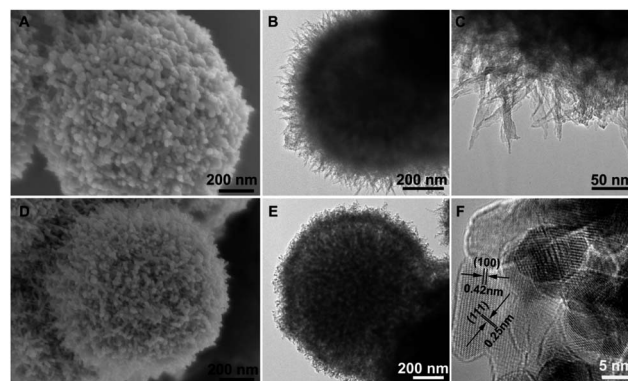

Fig. 3 SEM and TEM images of the $K_{0.27}MnO_2 \cdot 0.54H_2O$–Co salts/CNT and Mn_3O_4–CoO/CNT nanocomposites.

$2p_{1/2}$ spin-orbit peaks of Mn are located at 641.6 and 653.4 eV, respectively (Fig. 4C). The splitting width (11.8 eV) between the Mn $2p_{1/2}$ and $2p_{3/2}$ peaks is in accordance with the literature.[29,30] The Co 2p spectrum shows a doublet consisting of a low energy band (Co $2p_{3/2}$ at 780. 2 eV) and a high energy band (Co $2p_{1/2}$ at 795.7 eV) (Fig. 4D), consistent with that of Co_3O_4,[6,7] since the conversion of CoO to Co_3O_4 likely occurred on the surface of the nanoparticles.

To assess their ORR catalytic activity, the electrode materials were loaded (with equal mass loading) onto the GCE. The electrodes were interrogated by cyclic voltammetry (CV) in

O_2- and for reference, N_2-saturated 0.1 M KOH solutions, and the data are shown in Fig. 5A. The ORR peak of the Mn_3O_4–CoO/CNT nanocomposite electrode shifted to a more positive potential, e.g., $\sim$−0.082 V, in contrast to $\sim$−0.136 V for Mn_3O_4/CNT and $\sim$−0.095 V for CoO/CNT. This reveals that the Mn_3O_4–CoO/CNT catalysts exhibited better ORR catalytic activity than the Mn_3O_4/CNT and CoO/CNT catalysts, and closely approached that of the commercial Pt/C (10 wt%) catalyst, which is the gold standard for the ORR catalysts.

The ORR kinetics can be observed from the linear sweep voltammetry (LSV) curves in Fig. 5B, which were investigated
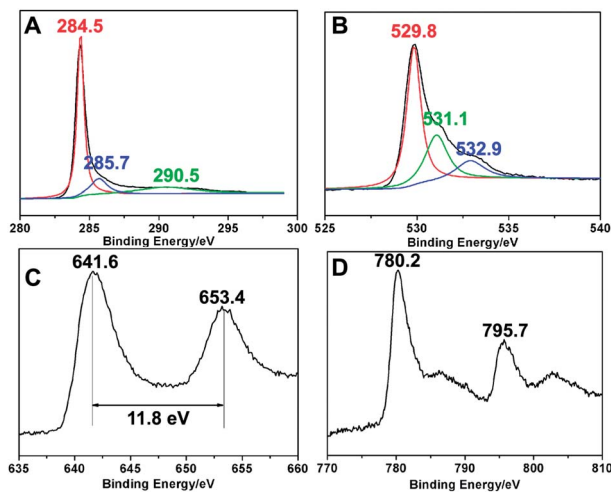
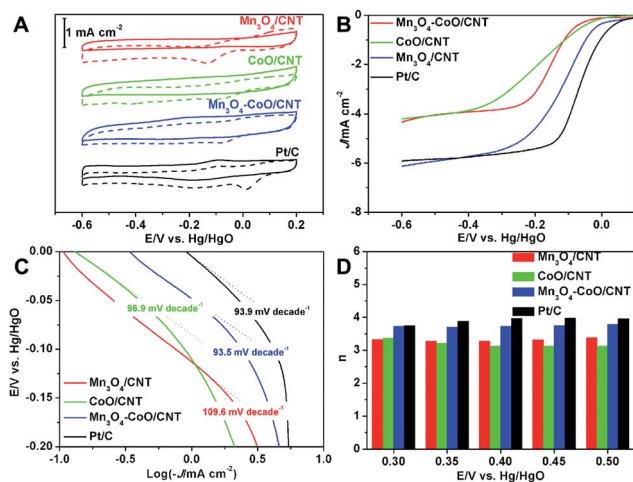**Fig. 4** XPS spectra of C 1s, O 1s, Mn 2p and Co 2p of the Mn_3O_4–CoO/CNT nanocomposites.

Fig. 5 The ORR catalytic activity of the Mn_3O_4/CNT, CoO/CNT, Mn_3O_4–CoO/CNT and commercial Pt/C catalysts: (A) CV curves in N_2-(solid line) or O_2-saturated 0.1 M KOH (dashed line), (B) rotating-disk voltammograms at a rotation rate of 2400 rpm in O_2-staturated 0.1 M KOH, (C) Tafel plots at a rotation rate of 2400 rpm in O_2-staturated 0.1 M KOH, and (D) electron transfer number (n) profiles obtained from rotating disk voltammograms at different rotation rates in Fig. SI-6.†

using the rotating-disk electrode (RDE) technique in O_2-saturated 0.1 M KOH electrolyte. We can see that the ORR process is controlled by the kinetic process, the mixed diffusion-kinetic process and the diffusion process in the potential ranges of −0.10 to 0 V, −0.20 to −0.10 V, and less than −0.20 V, respectively. In the kinetic controlled region, the Mn_3O_4–CoO/CNT electrodes exhibited a higher onset potential (−0.02 V) than the Mn_3O_4/CNT and CoO/CNT electrodes, which is slightly less than that of the commercial Pt/C catalyst (0.02 V). The half wave-potentials in the mixed diffusion-kinetic controlled region follow a similar tendency to the onset potentials, in the sequence of Pt/C (−0.062 V) > Mn_3O_4–CoO/CNT (−0.116 V) > Mn_3O_4/CNT (−0.148 V) > CoO/CNT (−0.186 V). In the

diffusion-controlled region, the diffusion-limited current densities of the Mn_3O_4–CoO/CNT electrodes approach that of the Pt/C catalyst at high overpotentials, which highly exceed those of the Mn_3O_4/CNT and CoO/CNT electrodes. Together, these results further confirm that the Mn_3O_4–CoO/CNT composite catalysts showed better ORR catalytic activity than the Mn_3O_4/CNT and CoO/CNT catalysts.

The ORR catalytic activity of these catalysts can also be evaluated from the Tafel slopes in Fig. 5C, calculated from the E versus log(−J) curves in O_2-saturated 0.1 M KOH aqueous solution. The Tafel slope reveals the value of the transfer coefficient for the given direction of the electrode reaction, which means that shallower Tafel slopes correspond to better ORR catalytic activity. The Mn_3O_4–CoO/CNT catalysts exhibited a Tafel slope of 93.5 mV per decade at over-potentials from 0.00 to −0.10 V, close to that of the commercial Pt/C catalyst (93.9 mV per decade) and lower than the Mn_3O_4/CNT (109.6 mV per decade) and CoO/CNT (96.9 mV per decade) catalysts.

A series of rotating disk voltammograms of the ORR in O_2-saturated 0.1 M KOH electrolyte catalysed by commercial Pt/C and the nanocomposite catalysts were measured, and are shown in Fig. SI-6.† After being analysed using the Koutecky–Levich equation (eqn (1) in the experimental section), a plot of the inverse current density J^{-1} versus $\omega^{-1/2}$ yielded a straight line with the intercept corresponding to J_k and the slope reflecting the so-called B factor (inset of Fig. SI-6†). The electron transfer number (n) can be calculated from the B factor, according to eqn (2) (see the experimental section), as shown in Fig. 5D. The linearity of the Koutecky–Levich plots and the near parallelism of the fitting lines are consistent with first-order reaction kinetics with respect to the concentration of the dissolved oxygen, and implicate the similar electron transfer numbers for the ORR at different potentials in the region of −0.30 to −0.50 V. The ORR electron transfer numbers in Fig. 5D are calculated as less than 3.5 for the Mn_3O_4/CNT and CoO/CNT catalysts, suggesting the incomplete reduction of oxygen. Meanwhile, the Mn_3O_4–CoO/CNT catalysts catalysed the ORR via a complete $4e^-$ reaction, in much the same way as a high-quality commercial Pt/C catalyst does, which is impressive for a non-Pt catalyst.

The above results indicate that O_2 molecules are primarily reduced on the Mn_3O_4/CNT and CoO/CNT catalysts via an incomplete oxygen reduction process. It can be supposed that, on the Mn_3O_4–CoO/CNT catalysts, O_2 molecules are initially catalysed into the intermediate product HO_2^- ions by the exterior CoO catalytic active sites, and then are diffused into the interior Mn_3O_4 catalytic active sites to be further reduced into OH^- ions. Thus, a complete oxygen reduction reaction is carried out on the Mn_3O_4–CoO/CNT catalysts. The Mn_3O_4–CoO/CNT catalysts also exhibited a higher onset potential and shallower Tafel slope than the Mn_3O_4/CNT and CoO/CNT catalysts. In short, owing to the synergistic catalytic effect of the Mn_3O_4 and CoO active sites, the Mn_3O_4–CoO/CNT catalysts exhibited better ORR catalytic activity.

The cycle stability is another important performance metric for ORR catalysts. Fig. 6A shows the chronoamperometric response curve polarized at a constant voltage of −0.40 V in
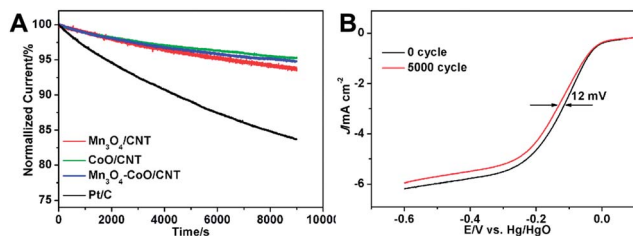
3798 | J. Mater. Chem. A, 2014, **2**, 3794–3800

This journal is © The Royal Society of Chemistry 2014

Fig. 6 Cycle stability performance of the nanocomposite and commercial Pt/C catalysts: (A) chronoamperometric responses (percentage of current retained *versus* operation time) kept at −0.40 V *versus* the Hg/HgO reference electrode in O_2-saturated 0.1 M KOH electrolyte at a rotating rate of 2400 rpm, and (B) RDE voltammograms for the ORR at the Mn_3O_4–CoO/CNT catalysts after 5000 cycles at a rotation rate of 2400 rpm.

O_2-saturated 0.1 M KOH electrolyte. The commercial Pt/C catalyst exhibited a ∼16.3% decrease in the current density after 9000 s. By contrast, the nanocomposite catalysts showed excellent cycle stability. For example, the ORR current densities have a retention ratio of 93.6% for Mn_3O_4/CNT, 95.2% for CoO/CNT and 94.8% for Mn_3O_4–CoO/CNT tested under the same conditions. Even after 5000 cycles of a durability test, the half-wave potential of the polarization curve for the Mn_3O_4–CoO/CNT nanocomposite catalysts only decreased by 12 mV, as shown in Fig. 6B.

The catalytic activity for CO oxidation on the CoO/CNT, Mn_3O_4/CNT and Mn_3O_4–CoO/CNT catalysts was investigated, as shown in Fig. 7. The CNTs in the composites are very stable at <250 °C in the presence of an oxygen atmosphere, as can be seen from the TGA results (Fig. SI-7†), and thus have no influence on the conversion efficiency of the CO oxidation. The CoO/CNT catalysts show initial and complete conversion temperatures of 120 and 160 °C, respectively. The catalytic activity was close to Co_3O_4 nanocubes and octahedrons with exposed {100} and {111} faces, and inferior to Co_3O_4 nanorods with exposed {110} faces,[7] since the catalytically active sites for CO oxidation are

supposed to be Co^{3+} sites rather than Co^{2+} sites.[19–22] The Mn_3O_4/CNT catalysts show initial and complete conversion temperatures of 80 and 220 °C, respectively, which suggests much better catalytic activity than the Mn_3O_4 catalysts reported previously.[31] The good catalytic activity is mainly ascribed to the mesoporous structure and high specific surface area (186.2 $m^2\ g^{-1}$), which provide many more catalytically active sites and favour molecule accessibility to the active surface of the nanocrystals and mass transport. After growing CoO on the Mn_3O_4/CNT composites, the initial and complete conversion temperatures decrease to 30 and 120 °C, respectively, and the temperature for 50% conversion of CO is much lower than for the CoO/CNT and Mn_3O_4/CNT composites. As compared with the Mn_3O_4/CNT catalysts, although its specific surface area decreased to 138.9 $m^2\ g^{-1}$, the improvement of the catalytic activity of the Mn_3O_4–CoO/CNT catalysts should be closely related to their different components. Thus, the co-contribution of the Mn_3O_4 and CoO catalytically active sites results in higher catalytic activity.

To characterize the reducibility of the Mn_3O_4/CNT, CoO/CNT and Mn_3O_4–CoO/CNT composites, the H_2-temperature programmed reduction (H_2-TPR) was investigated, and is presented in Fig. 8. The hydrogen consumption was for the stepwise reduction of cobalt oxide *via* $Co^{3+} \rightarrow Co^{2+} \rightarrow Co^0$, in the temperature range of 150–350 °C.[32–34] We know from the XPS results that Co^{3+} ions existed on the surface of the CoO/CNT composites due to the surface oxidation. Thus, a shoulder at ∼182 °C, which belongs to the reduction of Co^{3+} to Co^{2+}, appeared in the H_2-TPR curve. The temperature at ∼270 °C corresponds to the reduction of Co^{2+} to Co^0. In the H_2-TPR curve of the Mn_3O_4/CNT composites, the peak at ∼420 °C should be assigned to the reduction of Mn_3O_4 to MnO.[24,25] The broad peak at over 500 °C should be ascribed to the reduction of CNTs in the composites. After growing CoO on the Mn_3O_4/CNT composites, the reduction temperature of Mn_3O_4 to MnO on the Mn_3O_4–CoO/CNT composites shifts to a lower temperature
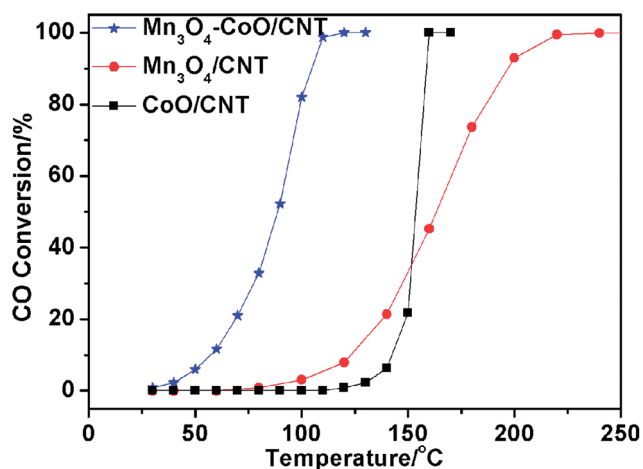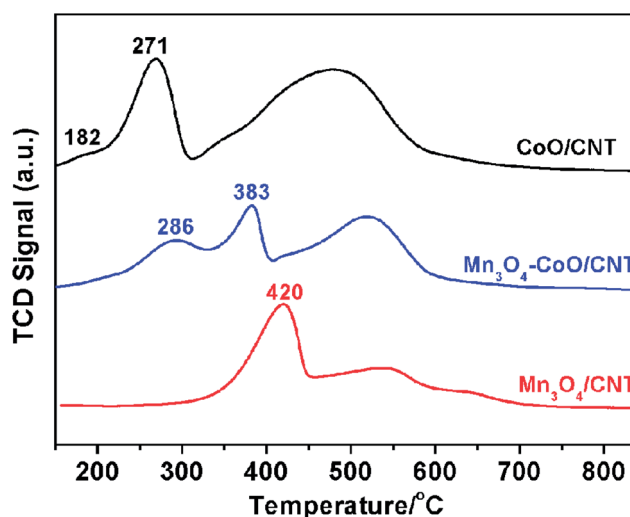

Fig. 7 Catalytic properties of the CoO/CNT, Mn_3O_4/CNT and Mn_3O_4–CoO/CNT nanocomposites, in the catalytic oxidation of CO, as a function of temperature.

Fig. 8 H_2-TPR profiles of the Mn_3O_4/CNT, CoO/CNT and Mn_3O_4–CoO/CNT composites.

This journal is © The Royal Society of Chemistry 2014

J. Mater. Chem. A, 2014, **2**, 3794–3800 | **3799**

(383 °C). This was probably because the CoO species interacted with Mn_3O_4, and the reducibility caused at relatively low temperatures may result in enhanced activity for CO oxidation, which is consistent with the CO conversion results.

Conclusions

In summary, a facile method was explored for synthesizing mesoporous Mn_3O_4–CoO spheres with a core–shell structure and wrapped by carbon nanotubes, as catalysts for the oxygen reduction reaction (ORR) and CO oxidation. Owing to the high specific surface area (138.9 m^2 g^{-1}), mesoporous structure and the cooperation of Mn_3O_4 and CoO catalytic active sites, the high catalytic activity and durability of the Mn_3O_4–CoO/CNT nanocomposite catalysts was demonstrated by comparison with the activity and durability of Mn_3O_4/CNT and CoO/CNT catalysts. The procedure explored in this study can be further developed as a generalized process that can be used to synthesize mixed metal oxide catalysts, for realizing advanced catalytic systems with enhanced performance.

Acknowledgements

Notes and references

1 H. A. Gasteiger, S. S. Kocha, B. Sompalli and F. T. Wagner, *Appl. Catal., B*, 2005, **56**, 9–35.
2 G. Wu, K. L. More, C. M. Johnston and P. Zelenay, *Science*, 2011, **332**, 443–447.
3 M. Lefevre, E. Proietti, F. Jaouen and J. P. Dodelet, *Science*, 2009, **324**, 71–74.
4 J. Suntivich, H. A. Gasteiger, N. Yabuuchi, H. Nakanishi, J. B. Goodenough and Y. Shao-Horn, *Nat. Chem.*, 2011, **3**, 546–550.
5 Y. Liang, Y. Li, H. Wang, J. Zhou, J. Wang, T. Regier and H. Dai, *Nat. Mater.*, 2011, **10**, 780–786.
6 J. Xu, P. Gao and T. S. Zhao, *Energy Environ. Sci.*, 2012, **5**, 5333–5339.
7 J. W. Xiao, Q. Kuang, S. H. Yang, F. Xiao, S. Wang and L. Guo, *Sci. Rep.*, 2013, **3**, 2300–2307.
8 J. W. Xiao, G. L. Xu, S. G. Sun and S. H. Yang, *Part. Part. Syst. Charact.*, 2013, **10**, 893–904.
9 K. P. Gong, F. Du, Z. H. Xia, M. Durstock and L. M. Dai, *Science*, 2009, **323**, 760–764.
10 S. Guo, S. Zhang, L. Wu and S. Sun, *Angew. Chem., Int. Ed.*, 2012, **51**, 11770–11773.
11 Y. Y. Liang, H. L. Wang, P. Diao, W. Chang, G. S. Hong, Y. G. Li, M. Gong, L. M. Xie, J. G. Zhou, J. Wang, T. Z. Regier, F. Wei and H. J. Dai, *J. Am. Chem. Soc.*, 2012, **134**, 15849–15857.
12 L. Q. Mao, T. Sotomura, K. Nakatsu, N. Koshiba, D. Zhang and T. Ohsaka, *J. Electrochem. Soc.*, 2002, **149**, A504–A507.
13 Y. Gorlin and T. F. Jaramillo, *J. Am. Chem. Soc.*, 2010, **132**, 13612–13614.
14 F. Y. Cheng, Y. Su, J. Liang, Z. L. Tao and J. Chen, *Chem. Mater.*, 2010, **22**, 898–905.
15 W. Xiao, D. L. Wang and X. W. Lou, *J. Phys. Chem. C*, 2010, **114**, 1694–1700.
16 Y. Gorlin, C. J. Chung, D. Nordlund, B. M. Clemens and T. F. Jaramillo, *ACS Catal.*, 2012, **2**, 2687–2694.
17 Y. L. Cao, H. X. Yang, X. P. Ai and L. F. Xiao, *J. Electroanal. Chem.*, 2003, **557**, 127–134.
18 F. H. B. Lima, M. L. Calegaro and E. A. Ticianelli, *Electrochim. Acta*, 2007, **52**, 3732–3738.
19 L. Hu, K. Sun, Q. Peng, B. Xu and Y. Li, *Nano Res.*, 2010, **3**, 363–368.
20 J. Jansson, A. E. C. Palmqvist, E. Fridell, M. Skoglundh, L. Osterlund, P. Thormahlen and V. Langer, *J. Catal.*, 2002, **211**, 387–397.
21 Y. Sun, P. Lv, J. Y. Yang, L. He, J. C. Nie, X. W. Liu and Y. D. Li, *Chem. Commun.*, 2011, **47**, 11279–11281.
22 X. W. Xie, Y. Li, Z. Q. Liu, M. Haruta and W. J. Shen, *Nature*, 2009, **458**, 746–749.
23 S. H. Liang, F. T. G. Bulgan, R. L. Zong and Y. F. Zhu, *J. Phys. Chem. C*, 2008, **112**, 5307–5315.
24 K. Ramesh, L. W. Chen, F. X. Chen, Y. Liu, Z. Wang and Y. F. Han, *Catal. Today*, 2008, **131**, 477–482.
25 L. C. Wang, Q. Liu, X. S. Huang, Y. M. Liu, Y. Cao and K. N. Fan, *Appl. Catal., B*, 2009, **88**, 204–212.
26 Y. Y. Liang, H. L. Wang, J. G. Zhou, Y. G. Li, J. Wang, T. Regier and H. J. Dai, *J. Am. Chem. Soc.*, 2012, **134**, 3517–3523.
27 D. Yan, P. X. Yan, G. H. Yue, J. Z. Liu, J. B. Chang, Q. Yang, D. M. Qu, Z. R. Geng, J. T. Chen, G. A. Zhang and R. F. Zhuo, *Chem. Phys. Lett.*, 2007, **440**, 134–138.
28 J. W. Xiao and S. H. Yang, *J. Mater. Chem.*, 2012, **22**, 12253–12262.
29 C. D. Wagner, W. M. Riggs, L. E. Davis and J. F. Moulder, *Handbook of X-Ray Photoelectron Spectroscopy*, Perkin Elmer Corporation, Eden Prairie, Minnesota, 1995.
30 J. W. Lee, A. S. Hall, J.-D. Kim and T. E. Mallouk, *Chem. Mater.*, 2012, **24**, 1158–1164.
31 C. Zhang, L. Han, W. Liu, H. X. Yang, X. Y. Zhang, X. F. Liu and Y. Z. Yang, *CrystEngComm*, 2013, **15**, 5150–5155.
32 M. F. Luo, Y. J. Zhong, X. X. Yuan and X. M. Zheng, *Appl. Catal., A*, 1997, **162**, 121–131.
33 H. Wang, H. Zhu, Z. Qin, G. Wang, F. Liang and J. Wang, *Catal. Commun.*, 2008, **9**, 1487–1492.
34 L. F. Liotta, G. Di Carlo, G. Pantaleo, A. M. Venezia and G. Deganello, *Appl. Catal., B*, 2006, **66**, 217–227.